ACCSCIENCE PUBLISHING

Engineering Science in Additive Manufacturing

ORIGINAL RESEARCH ARTICLE

Thermal-shield metastructures for routing heat flux in lightweight, high-efficiency heat sinks for multi-hotspot electronics

Kyungbeom Seo†, Sooyeon Ji†, Myounggi Hong, Yeonbin Seong, Yong Choi, Hwanju Lim, and Wonjoon Choi*

School of Mechanical Engineering, Korea University, 145 Anam-Ro, Seongbuk-Gu, Seoul, Republic of Korea

Abstract

The continuing miniaturization and increasing power density of electronic and optoelectronic devices have made compact, lightweight, reliable heat dissipation challenging, particularly for boards with many discrete hotspots. Conventional finned heat sinks reject heat in an isotropic, undirected manner; therefore, much of the fin volume far from the active sources contributes little to convection but adds mass and occupies space. In this work, we embedded a thermal-shield metastructure into the fin field to convert a conventional sink into a heat-flux-routing device that concentrated conductive heat flow into prescribed regions, so fins were installed only where they are useful. Building on transformation-thermotics-inspired unit-cell thermal shifters formed by alternating high- and low-conductivity layers, we used the thermal-shield concept to prescribe a heat-routing fin layout, *i.e.*, a metastructured ("meta-fin") sink whose fins populate only the shield-defined region of a multi-hotspot module. Using transient three-dimensional finite-element heat-transfer simulations with prescribed convective boundary conditions, we compared it with pin- and plate-fin baseline sinks matched in surface area or volume and weight. The simulations showed that the meta-fin increased the surface-utilization efficiency by >10% relative to the full-footprint pin- and plate-fin baselines and exhibited 15%–25% higher transient heat rejection across the comparison set, while reducing material volume and mass by ~45% relative to the full-footprint baselines. Thus, its mass-normalized transient heat rejection was ~2× that of a conventional sink. It additionally enabled control of the on-chip temperature landscape, producing a diagonal temperature contrast more than 2.5× that of the conventional full-footprint designs. These improvements arise from redesigning the fin layout rather than introducing new functional materials. Moreover, rapid advances in additive manufacturing and 3D printing provide practical fabrication routes for such unconventional heat-sink form factors, supporting the future demonstration, refinement, and deployment of metastructure-based thermal management.

Keywords: Thermal metamaterial; Thermal shield; Heat-flux control; Heat sink; Multi-hotspot electronics cooling; Lightweight thermal management; Additive manufacturing; 3D printing

†*These authors contributed equally to this work.*

***Corresponding author:**
Wonjoon Choi
(wojchoi@korea.ac.kr)

Citation: Seo K, Ji S, Hong M, *et al*. Thermal-shield metastructures for routing heat flux in lightweight, high-efficiency heat sinks for multi-hotspot electronics. *Eng Sci Add Manuf.* 2026;2(3):026300014. doi: 10.36922/ESAM026300014

Received: July 23, 2026

Revised: August 18, 2026

Accepted: August 20, 2026

Published online: August 27, 2026

Copyright: © 2026 Author(s). This is an Open-Access article distributed under the terms of the Creative Commons Attribution License, permitting distribution, and reproduction in any medium, provided the original work is properly cited.

Publisher's Note: AccScience Publishing remains neutral with regard to jurisdictional claims in published maps and institutional affiliations.

1. Introduction

Thermal management has become a principal constraint on the performance, reliability, and lifetime of modern electronic and optoelectronic systems. As devices continue to shrink while their power density increases, the heat generated per unit area has climbed steeply. Additionally, the limited internal volume available for heat to escape makes localized overheating increasingly difficult to avoid.[1,2] Elevated junction temperatures degrade electrical performance and accelerate failure mechanisms; further, because the coefficients of thermal expansion (CTE) of adjacent materials differ, these high junction temperatures generate thermo-mechanical stresses that threaten long-term durability.[2,3] These problems are most acute on contemporary circuit boards that carry multiple discrete heat sources, such as light-emitting-diode (LED) arrays, power electronic modules, and 2.5D/three-dimensional (3D)-integrated packages, where neighboring components interact thermally and produce strongly non-uniform temperature fields.[1,4]

Finned heat sinks remain the most widely used hardware for dissipating this heat owing to their structural simplicity, low cost, and reliable, maintenance-free operation.[3,5] By extending the surface area available for convection, fins—most commonly in the form of pins or plates—transfer heat conducted through the base into the surrounding air. A large body of work has sought to push this classical concept further by geometrically optimizing the fin shape, spacing, and arrangement[5]; micro/mini-channel and jet-impingement cooling[1,2]; and composites containing a phase change material and metal foam.[6] More recently, topology optimization has been combined with additive manufacturing, which can roughly double the thermohydraulic conductance of a sink relative to that of conventional rectangular fins.[7,8] Indeed, additive manufacturing (3D printing) has emerged as a transformative platform for thermal-management hardware in general, offering a geometric design freedom that conventional subtractive fabrication cannot match.[9,10] Building on this freedom, additive manufacturing has enabled lattice and triply periodic minimal-surface heat sinks[11], topology-optimized microchannel and conjugate designs[12,13], machine-learning- and surrogate-based design accelerators[14,15], and natural-convection heat sinks for immersion cooling.[16] Nonetheless, liquid cold plates and minichannel sinks remain the workhorses for high-flux electronics.[17,18] Despite this progress, sufficiently dissipating heat within tight volume and weight budgets remains a central bottleneck for compact electronics.[3,5]

Conventional optimization of fin shape, spacing, and arrangement generally improves heat-transfer area and convective performance while retaining an isotropically conducting base. More advanced approaches, including heat-path optimization and topology optimization, can intentionally redistribute conductive material and geometrical features to reduce thermal resistance or peak temperature, while high-conductivity spreaders such as engineered graphite architectures promote rapid lateral redistribution of heat. These strategies are highly effective, but their underlying design philosophy differs from that adopted here. In optimization-based approaches, the heat-flow pathway generally emerges as a consequence of minimizing a prescribed objective function, whereas high-conductivity spreading primarily seeks to reduce resistance and homogenize the temperature field. By contrast, the thermal-metastructure approach begins with a prescribed heat-flux function: regions through which heat should preferentially flow, as well as regions from which heat should be diverted, are defined in advance through anisotropic heat-flux steering. In the present heat-sink implementation, this prescribed field is translated into a routed fin layout so that convective surface is placed preferentially along the thermally active region. This distinction is particularly relevant to multi-hotspot electronics, where maximizing heat spreading alone may not be sufficient because thermal crosstalk and temperature-sensitive neighboring components must also be considered.

Thermal metamaterials provide exactly this capability. Following the introduction of transformation thermotics and the demonstration of shaped graded media with an apparently negative thermal conductivity[19], and inspired by earlier successes in transformation optics and acoustics[20-22], artificial thermal structures have been engineered to steer conductive heat flux at will, realizing cloaks, concentrators, rotators, and camouflage devices with no natural analog.[23-26] The field has matured rapidly since then: comprehensive frameworks and roadmaps have now advanced it from static cloaks, concentrators, and rotators[24,27] to dynamic, reconfigurable, and convective devices[28-30], spanning analytically designed complex metadevices[31], the manipulation of coupled mass and energy diffusion[32], non-Fourier wave-like heat transport[33,34], convective thermal cloaks for moving media[35,36], and fully 3D heat-routing architectures.[37,38] Further, data-driven and machine-learning methods have begun to automate the inverse design of such structures.[39] Crucially, for engineering purposes, this body of work has shown that heat can be guided along deterministic paths rather than being allowed to diffuse uniformly.[4,24]

However, translating these ideas into practical thermal hardware has been hindered by fabrication; ideal transformation-based media require continuously graded,

often singular, anisotropic properties that are difficult to manufacture.[4] Encouragingly, rapid advances in additive manufacturing—particularly metal and multi-material 3D printing—are steadily closing this fabrication gap; indeed, architectures that pair a single printable metal with engineered air gaps, such as those considered here, are directly compatible with established additive processes.[40-42] A productive alternative is to discretize the required heat-flux field into assemblies of simple, easy-to-manufacture unit cells, so-called "thermal shifters" built from two alternating media of contrasting conductivity, whose layer orientation bends heat flux on demand.[4,43] Our group previously showed that the programmed reassembly of such unit cells can realize shield, concentrator, diffuser, and rotator functions on a single platform.[43] Reviews of thermal metamaterials for electronic packaging have since argued that precisely this type of deterministic heat guidance could mitigate crosstalk and protect temperature-sensitive components in high-density packages.[4] However, the use of this previously established thermal-shield concept as a design rule for selectively placing heat-sink fins, and the resulting thermal and mass benefits relative to conventional fin layouts, have not been quantitatively examined.

Here, we report a metastructured heat sink that embeds the thermal-shield function directly into its fin layout, thereby converting a conventional finned sink into a compact heat-flux-routing device for multi-hotspot electronics. Building on the previously established thermal-shifter and thermal-shield framework, the present study translates the shield-derived heat-routing pattern into a practical design rule for heat-sink fin placement in a multi-hotspot system. Specifically, we laid out the fins of a heat sink for a 17-element multi-hotspot module such that they populate only the region into which the conductive heat flux is routed, leaving the remainder of the base unfinned. Importantly, the heat-transfer model represents the metastructure through its macroscopic design consequence—the routed fin layout—rather than by resolving the sub-cell layered anisotropy as a graded conductivity tensor. The shield analyses in sections 2.1 and 2.2 serve to justify the fin placement. Using transient 3D finite-element heat-transfer simulations with prescribed convective boundary conditions, we compared this meta-fin sink with conventional pin- and plate-fin baseline sinks under two controlled comparisons: one matching the surface area (the baseline sinks labeled with the suffix "_all") and one matching the volume and weight (the baseline sinks labeled with the suffix "_center"); thereby, isolating the role of the fin layout from trivial geometric effects. We showed that the meta-fin essentially utilized its entire fin surface for convection, raising the surface-utilization efficiency by more than 10% and transient heat rejection by 15%–25%, while being approximately 45% smaller and lighter, roughly doubling the heat rejected per unit mass. Because this gain is achieved by redesigning the fin layout rather than introducing new functional materials, the proposed geometry can be realized using metal additive manufacturing or precision computer numerical control (CNC) machining, both of which are suitable for producing non-standard fin and void patterns. Thus, it offers a practical route toward lightweight, crosstalk-aware heat sinks for multi-hotspot electronics.

2. Concept and theoretical framework

2.1. Governing equations and the transformation-thermotics background

The behavior of each configuration in this study is governed by the heat-diffusion equation. In a solid of density ρ, specific heat c_p, temperature gradient ∇T, and thermal-conductivity tensor κ, conservation of energy gives:

$$\rho\, c_p\, \partial T/\partial t = \nabla\cdot(\kappa \cdot \nabla T) + \dot{q}, \tag{1}$$

where q is the volumetric heat-generation rate, and the conductive heat flux obeys the anisotropic Fourier law:

$$q = -\,\kappa \cdot \nabla T. \tag{2}$$

In an ordinary isotropic material, $\kappa = k \cdot I$, where k is the scalar thermal conductivity, and I is the identity tensor. Heat then diffuses down the local temperature gradient and spreads outward from the source without prescribed directional control. This is the behavior of a conventional heat sink. The central premise of transformation thermotics is that this isotropic diffusion can be intentionally reshaped by spatially tailoring κ. Formally, if a reference temperature field is deformed by a coordinate transformation with the Jacobian matrix J, the steady diffusion equation retains its form, provided that the conductivity is mapped according to:

$$\kappa' = (J\, \kappa\, J^T) \,/\, det(J). \tag{3}$$

To prescriptively reshape the heat-flux lines (*e.g.*, bending them around a region to shield it), the conductivity κ' must generally be continuously graded, strongly anisotropic, and sometimes singular, which is difficult to directly manufacture.[19,20,22] The practical solution adopted in this study follows the unit-cell-shifter approach[4,43]; specifically, the required anisotropy is approximated piecewise with a small set of simple, layered, two-material cells, each supplying a locally uniform but strongly anisotropic conductivity. The following subsection summarizes the relevant anisotropic heat-transfer relations and shows how the resulting shield pattern is used to define the fin layout in the present study.

2.2. Heat-flux routing with layered thermal-shield unit cells

The thermal-shield architecture used as the design basis in this study follows the previously established layered unit-cell approach and is composed of metal–air thermal-shifter cells, as illustrated in Figure 1. Each cell is a periodic stack of alternating thin layers of a high-conductivity metal (aluminum in the present heat-sink design; the earlier shield prototype shown in Figure 1a was fabricated in copper) and low-conductivity air gaps with thicknesses d_h and d_l, respectively, arranged at 45° from the cell edges.[43] Treating the stack using the effective-medium (homogenization) theory, the heat flowing parallel to the layers experiences the two media as thermal resistances in parallel, whereas the heat flowing across them faces their resistances in series. Therefore, the limiting conductivity in parallel is the volume-weighted arithmetic mean:

$$k_{\parallel} = (k_h\, d_h + k_l\, d_l) / (d_h + d_l), \tag{4}$$

whereas across the layers in series, it is the harmonic mean:

$$k_{\perp} = (d_h + d_l) / (d_h/k_h + d_l/k_l), \tag{5}$$

where k_h and k_l (d_h and d_l) are the conductivities (thicknesses) of the high- and low-conductivity layers, respectively. These are the principal values of a diagonal conductivity tensor $\kappa_{cell} = \mathrm{diag}(k_{\parallel}, k_{\perp})$ expressed in the layer-aligned frame. When the cell is rotated by an angle θ (here θ = 45°) relative to the heat-sink axes, the laboratory-frame tensor $\kappa_{lab} = R(\theta)\, \kappa_{cell}\, R(\theta)^T$ acquires off-diagonal components:

$$k_{xx} = k_{\parallel} \cos^2\theta + k_{\perp} \sin^2\theta,\ k_{xy} = (k_{\parallel} - k_{\perp}) \sin\theta \cos\theta. \tag{6}$$

The off-diagonal term, k_{xy}, specifically tilts the heat-flux vector away from the temperature gradient in **Equation 2**, deflecting the heat that enters the cell toward the high-conductivity layer rather than allowing it to flow straight down the gradient. The magnitude of this deflection is governed by the anisotropy ratio:

$$\chi = k_{\parallel} / k_{\perp}, \tag{7}$$

which determines the strength of the heat-flux steering. Accordingly, the heat-routing strength depends on both the thermal-conductivity contrast between the constituent materials and their relative layer dimensions. The aluminum–air configuration adopted here provides a very large directional conductivity contrast and therefore represents a strong heat-routing condition suitable for demonstrating the present design concept. The unit-cell material combination and dimensions were selected as a representative configuration rather than independently optimized in this study. For the aluminum–air pairing and 45° geometry used in this study, evaluating the directional heat transfer through a single cell yields a ratio on the order of 10^3 between the easy and difficult directions, so that the heat injected at a certain point is funneled almost entirely along the high-conductivity direction. In this large-χ limit, the low-conductivity air gaps behave as near-adiabatic walls, forming a closed loop of cells that act as an effective thermal barrier enclosing the shielded region. Simultaneously, corridors are left between the barriers acting as preferential conduction paths that deliver heat to the locations chosen for the fins. By tiling cells of appropriate orientation around the source array, the heat flux can be wrapped around a chosen region and thermally isolated from its surroundings, *i.e.*, the "thermal shield" function.[43] Figure 1c shows the simulated results for a fin-free shield; heat from the multi-source array is confined to a diamond-shaped region within the plus-shaped envelope, leaving the surrounding base near ambient temperature. In the large-anisotropy regime (on the order of 10^3) considered here, the unit-cell orientations predominantly determine the macroscopic spatial envelope of preferential and suppressed heat flow, as demonstrated by the shield pattern in Figure 1c. The shield analysis is therefore used to determine the thermally active region in which the fins should be placed. The heat-sink simulations in sections 3 and 4 then model this macroscopic design consequence with conventional aluminum fins rather than re-resolving the layered anisotropy of each unit cell. This reduced-order representation preserves the dominant routing feature relevant to the present objective, such as the location and geometry of the heat-carrying fin region, while enabling a direct comparison of the resulting fin layout with conventional heat sinks.

2.3. Surface-utilization efficiency and its relation to fin theory

To compare the designs on a physically meaningful basis, we define the efficiency that measures the degree to which a heat sink uses its own surface for convection. The convective power rejected by a surface element of area A at the surface temperature T_s is:

$$Q = h\, A\, (T_s - T_{air}), \tag{8}$$

where h is the convective heat-transfer coefficient, and T_{air} is the ambient temperature. A given surface can dissipate the maximum amount of heat when every point on the surface sits at the junction (maximum) temperature T_{max}. Therefore, we define the surface utilization efficiency as the ratio of actual dissipation to ideal dissipation:

$$\eta = \iint_A [T(x,y) - T_{air}]\, dA \,/\, [A_{hs}\, (T_{max} - T_{air})], \tag{9}$$

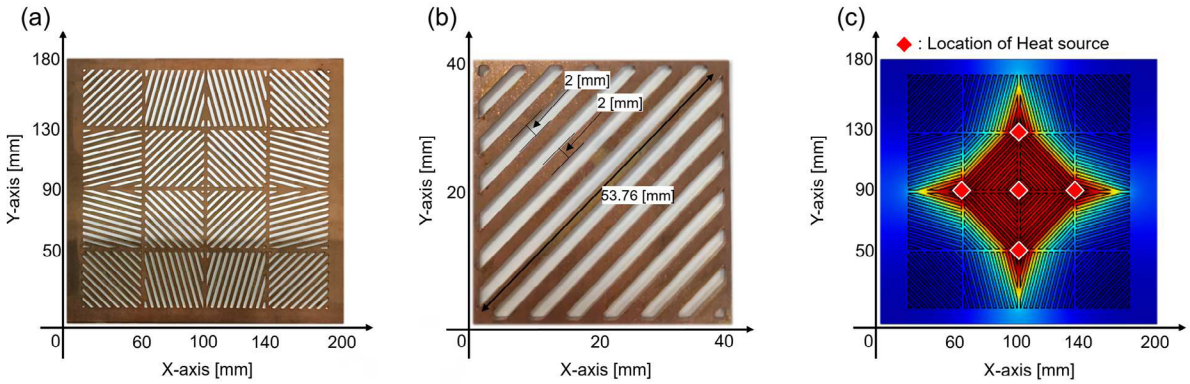

Figure 1. Thermal-shield concept. (a) Photograph of a fabricated fin-free thermal shield prototype (copper with air slots); (b) geometry of the 45° metal–air unit cell of the thermal shifter; (c) simulated temperature field showing heat from the multi-source array confined to a diamond-shaped region within the plus-shaped envelope, leaving the surroundings near ambient. This shield pattern defines where fins are placed in the meta-fin design.

where $T(x,y)$ is the local surface temperature, and A_{hs} is the total heat-sink surface area. By construction, η is dimensionless and bounded by unity. Specifically, η → 1 when the whole surface is isothermal at T_{max}, *i.e.*, when no fin area is "wasted" near ambient temperature. A sink that spreads heat into cold, distant fins has a low η even when its absolute surface area is large. Thus, improving η is precisely the role of the thermal shield.

Notably, η differs from the classical fin efficiency $\eta_f = \tanh(m{\cdot}L)/(m{\cdot}L)$, which measures how closely a single fin approaches operation entirely at its base temperature. As shown in section 2.4, the fins in this study are so short and conductive that $\eta_f \approx 1$ individually; the quantity that actually differs between the designs is therefore not the efficiency of each fin but whether heat is delivered to the fins at all. The surface-utilization efficiency η captures this system-level effect, folding the spatial temperature distribution into a single number. Another useful property follows from the linearity of **Equations 1** and **2**: when κ, h, and the geometry are fixed, and the boundary conditions are homogeneous in the temperature rise $\theta = T - T_{air}$, the field at any fixed time scales linearly with the source power, $\theta \propto \dot{q}$. The numerator and denominator of **Equation 9** then scale identically, so η is independent of the source intensity, which is exactly the load-independence that will be observed in section 4.2.

2.4. Dimensionless parameters and the transient energy balance

Three dimensionless groups clarify why the designs differ and justify the modeling parameters chosen in section 3. First, the Biot number based on a fin half-thickness, $Bi = h(t/2)/k$, is on the order of 10^{-4} for the aluminum fins considered here (h = 10 W m^{-2} K^{-1}, $t \approx$ 2–6 mm, k = 238 W m^{-1} K^{-1}). Such a small Biot number means that each fin is essentially isothermal across its cross-section. Further, internal conduction is far faster than surface convection, so the fins are not internally conduction-limited. Second, the fin parameter $m{\cdot}L$, with $m = \sqrt{(hP/kA_c)}$ and the fin height L = 10 mm, is likewise small ($m{\cdot}L \approx 0.05$), giving a single-fin efficiency $\eta_f = \tanh(m{\cdot}L)/(m{\cdot}L) \approx 0.999$. Individually, every fin in each design is almost perfectly efficient. Therefore, the performance differences discussed below cannot originate in the fins themselves; they must originate in the conduction path that delivers heat from the concentrated sources to the fin field, that is, in the base-spreading resistance, which is exactly what the routed metastructure is designed to reduce.

Third, the transient response is characterized by a thermal time scale $\tau \sim (\rho c_p V)/(hA)$, representing the ratio of the heat capacity of the sink to its convective conductance. Based on the material mass and total convecting surface area of each configuration, the characteristic times are approximately 361, 357, 196, 309, and 297 s for pin fin_all, plate fin_all, meta-fin, pin fin_center, and plate fin_center, respectively. During the transient response, the supplied energy is partitioned between convection and sensible storage according to the instantaneous energy balance:

$$Q_{in} = Q_{conv} + dE_{st}/dt = hA(\bar{T}_s - T_{air}) + \rho c_p V(d\bar{T}/dt), \quad (10)$$

where $\bar{T}$ denotes an appropriately averaged temperature. Two designs that receive the same input but differ in mass therefore reject different amounts of heat at the same instant: the lighter sink, having the smaller storage term $\rho c_p V(d\bar{T}/dt)$, diverts a larger share of the input to convection. This is the physical origin of the mass

dependence that will be discussed in section 4.3, and it is why a transient framework is necessary: at steady state ($t \gg \tau$), the storage term vanishes, and every design rejects its full input, eliminating the distinction. The metastructured sink simultaneously benefits both terms in **Equation 10**: it carries less mass, thus shrinking the storage term, and it delivers heat to a fully utilized, uniformly hot fin surface, thus enlarging the convective term.

2.5. Heat-sink configurations

Figure 2 shows the five configurations compared in this study. Two are conventional baseline sinks built on a plain base with fins covering the entire footprint: a pin-fin sink (pin fin_all, Figure 2a) and a plate-fin sink (plate fin_all, Figure 2b), which are the most common layouts in industry and are most frequently used as controls. The third is the metastructured sink (meta-fin, Figure 2c), whose fins populate only the diamond-shaped region into which the thermal shield in Figure 1 routes the heat, and the remaining base is left unfinned. To distinguish the effect of the shield-derived routing pattern from the simpler effects of concentrating fins near the heat-source region and reducing material mass, we introduced two additional mechanistic control sinks—pin fin_center (Figure 2d) and plate fin_center (Figure 2e). In these configurations, conventional isotropic pin or plate fins are placed within a fin-bearing region comparable to that of the meta-fin, while the surrounding base is perforated to match the material volume and mass of the meta-fin. These controls therefore represent a null hypothesis in which a similar amount of conventional fin material is concentrated near the sources without the shield-derived routing layout. The 17 heat sources are arranged in the plus-shaped pattern in Figure 2f, which is representative of the lattice-like source distributions found on LED and power electronic modules.

Because convective dissipation scales with the surface area whereas the thermal-storage behavior scales with mass, a fair comparison must control for both. We therefore tuned the fin pitch and thickness so that the two full-footprint baseline sinks and the meta-fin had nearly equal surface areas (Table 1) and independently tuned the perforation of the two center baseline sinks so that their volume and weight matched those of the meta-fin (Table 2). As summarized in Table 1, the surface areas of pin fin_all, plate fin_all, and meta-fin agree within ~2%. Moreover, as summarized in Table 2, the volumes and weights of the _center baseline sinks lie within ~1% of those of the meta-fin. Together, these two complementary control sets reduce the dominant surface-area and mass differences and allow the effect of the shield-derived layout to be assessed against conventional geometries under approximately matched conditions.

Table 1. Footprint, fin geometry, and total surface area of the surface-area-matched configurations (pin fin_all, plate fin_all, and meta-fin)

Model	Footprint (mm × mm)	Fin pitch, *s* (mm)	Fin thickness/diameter, *t* (mm)	Surface area (m^2)
Pin fin_all	163 × 163	8	6	0.13360
Plate fin_all	163 × 163	4	3	0.13318
Meta-fin	163 × 163	2	2	0.13572

Notes: The surface areas agree to within ~2%.

Table 2. Footprint, base-perforation geometry, volume, and weight of the volume- and weight-matched configurations (meta-fin, pin fin_center, and plate fin_center)

Model	Footprint (mm × mm)	Hole pitch (mm)	Hole size (mm)	Volume (cm^3)	Weight (kg)
Meta-fin	163 × 163	1	1	106	0.296
Pin fin_center	163 × 163	8	5	105	0.294
Plate fin_center	163 × 163	8	2	107	0.299

Notes: The volumes and weights agree to within ~1%.

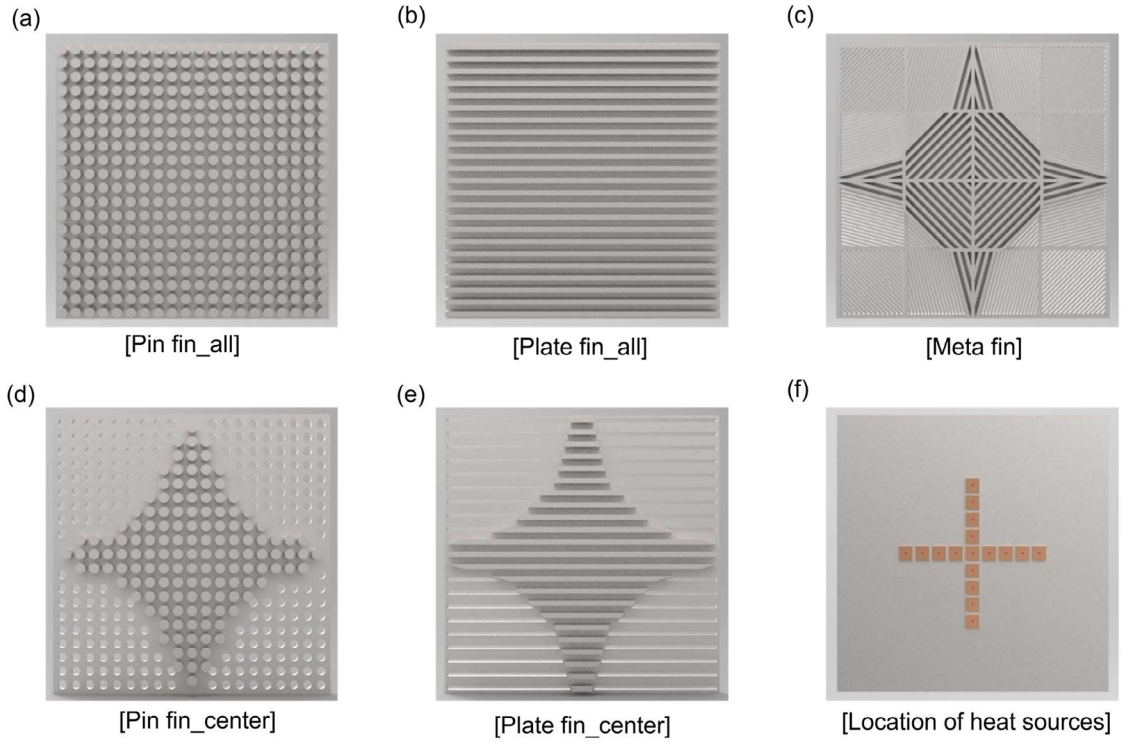

Figure 2. Five heat-sink configurations considered in the numerical analysis: (a) pin fin_all, (b) plate fin_all, (c) meta-fin, (d) pin fin_center, and (e) plate fin_center, together with (f) the 17-element plus-shaped heat-source layout. In the meta-fin, fins populate only the shield-routed region.

3. Numerical modeling

We evaluated the five configurations using transient 3D finite-element heat-transfer simulations (COMSOL Multiphysics), in which the solid conduction problem was solved under prescribed convective boundary conditions. A transient analysis is essential because, as shown below, the differences between the designs are governed not only by their steady convective capacity but also by how much of the supplied energy is temporarily stored in the sink as the temperature field develops. Figure 3a defines the geometry of the heat-source module and fin cross-section, and Figure 3b shows the computational domain and boundary conditions. Mesh independence was verified using the representative Pin fin_all configuration, as summarized in Table 3. Each sink has a 163 mm × 163 mm footprint, and the profile is low to suit thin electronic enclosures. Specifically, the aluminum fin base thickness H_b is 3 mm, and the aluminum fin height H_f is 10 mm. Each of the 17 heat-source modules comprises a 1 mm × 1 mm × 0.5 mm GaN die—representative of an LED or wide-bandgap power device[44]—mounted on an 8 mm × 8 mm × 1.6 mm copper substrate and bonded to the base through a thermal interface material (TIM). The geometry and thermophysical properties of each component are listed in Table 4.

A uniform heat flux was applied to the heat-source array, with the total applied heat-source power varied in five equal steps from 5 to 25 W. All exposed heat-sink surfaces are subjected to a prescribed convective boundary condition with T_{air} = 20 °C, and a uniform surface-averaged heat-transfer coefficient of h = 10 W m^{-2} K^{-1}. The model does not explicitly resolve the buoyancy-driven airflow around individual fins; rather, the common boundary condition is used to compare the solid-side temperature fields and transient energy partition produced by the different geometries. The bounding box is treated as an open boundary, and radiative exchange is neglected because of the low operating temperatures of the heat sinks and power sources. The transient solution was advanced from a uniform initial temperature of 20 °C, and the heat-rejection results presented below were evaluated at a common physical time of approximately t = 200 s after application of the heat load. Using the characteristic thermal time scales defined in Section 2.4, this corresponds to normalized times t/τ of approximately 0.55, 0.56, 1.0, 0.65, and 0.67 for pin fin_all, plate fin_all, meta-fin, pin

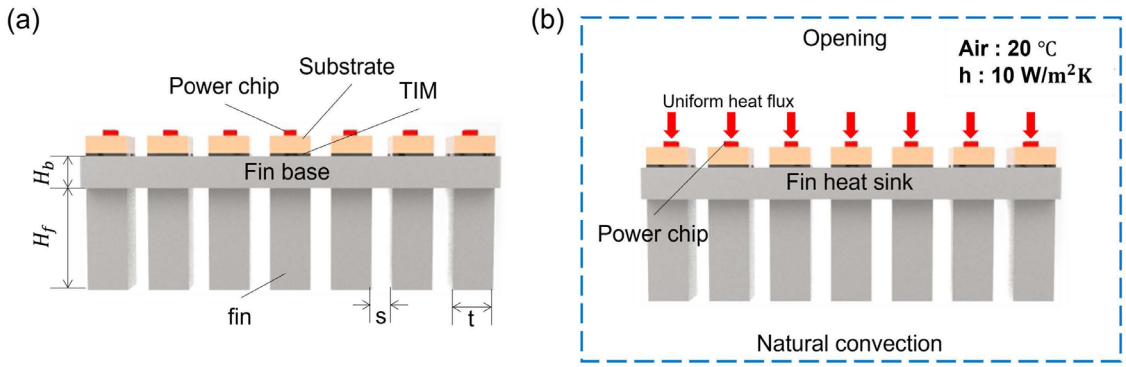

Figure 3. Multi-hotspot heat-sink geometry and computational framework. (a) Geometry of a heat-source module and the fin cross-section (base height H_b, fin height H_f, fin pitch s, and fin thickness/diameter t). (b) Computational domain and boundary conditions: a uniform heat flux from each die and a prescribed convective boundary condition to air at 20 °C with a uniform coefficient h. The model does not explicitly resolve buoyancy-driven airflow around the fins.

fin_center, and plate fin_center, respectively. Unless otherwise noted, the transient quantities reported below correspond to this common evaluation time. The spatial mesh was refined until the temperature field and convected power were insensitive to further refinement. A mesh-convergence analysis using the representative Pin fin_all configuration showed that further refinement beyond the selected M3 mesh (185,132 tetrahedral elements) changed the peak temperature by no more than 0.01K and the total convected power by less than 0.01%; therefore, the M3 mesh was adopted for the subsequent simulations. Identical heat loads, material properties, initial conditions, and prescribed boundary-condition definitions were applied to all configurations to isolate their solid-side geometric response within this common computational framework.

The comparison is made at this common transient evaluation time (Figure 4), when the supplied energy remains partitioned between convective heat rejection and sensible thermal storage. Because the governing conduction–convection problem is linear in the temperature rise (section 2.3), the temperature field—and with it the rejected power—scales proportionally with the source power; consequently, the percentage differences between the designs reported below are independent of the absolute temperature level. At higher loads, longer times, or under different convection conditions, the absolute temperatures and quantitative separation among the designs may change. The reported comparisons should therefore be interpreted within the prescribed boundary conditions considered here.

4. Results and discussion

4.1. Temperature fields and fin-surface utilization

Figure 4 shows the temperature fields of the five sinks at the common transient evaluation time and a representative source load. Essentially, in the two full-footprint baseline sinks (Figures 4a and 4b), heat spreads isotropically outward from the source array; only the central fins directly above the sources are appreciably heated, while the large peripheral fin area remains close to ambient. Such uniform spreading is useful for homogenizing the base temperature but it is inefficient for convective rejection because most of the installed fin surface operates at a small temperature difference from the air and therefore contributes little to heat dissipation. The metastructured sink behaves very differently (Figure 4c): because its fins occupy only the routed region, the heat reaches and essentially drives that entire region to a high, nearly uniform temperature; thus, the full fin surface participates in convection. Although the two _center baseline sinks (Figures 4d and 4e) occupy the same footprint as the meta-fin, they do not reproduce this behavior. Instead, heat concentrates at the center of the pin-fin cluster or leaks into the unfinned base of the plate-fin case, confirming that simply restricting the fin area is not sufficient. Meanwhile, the routed layout matched to the heat-flux pattern produces uniform, full-surface heating.

The contrast between the designs is best understood in terms of the resistance to thermal spreading. Heat enters each sink through the small (8 mm × 8 mm) source footprints and must spread laterally through the thin (3 mm) base before it can reach the fins, as established in section 2.4; this base-spreading resistance dominates the conduction path, not the resistance of the individual fins, which are essentially isothermal. In the pin fin_all and plate fin_all sinks, the heat spreads radially and isotropically; thus, their areal density, and hence the local base-to-air temperature difference, decays with the distance from the sources, leaving the outer fins underused. In the meta-fin, the routed corridors provide low-resistance conduction

Table 3. Mesh convergence analysis for the representative Pin fin_all configuration under a 10 W heat load

Mesh level	Elements (Tetrahedra)	T_{max} (K)	T_{max} (K)	Q_{conv} (W)	Q_{conv} (%)	Solver time
M1	25,557	302.54	0.05	9.9952	0.001	4 min 16 sec
M2	79,160	302.58	0.01	9.9957	0.006	8 min 16 sec
M3 (This work)	185,132	302.59	—	9.9951	—	15 min 33 sec
M4	425,374	302.60	0.01	9.9955	0.004	29 min 24 sec
M5	928,861	302.60	0.01	9.9946	0.005	49 min 40 sec

Notes: The total number of tetrahedral elements, peak temperature (T_{max}), total convected power (Q_{conv}), and solver time are reported for five mesh-refinement levels. The changes in T_{max} and Q_{conv} are calculated relative to the selected mesh level (M3).

Table 4. Geometry and thermophysical properties of the heat-sink and heat-source-module components used in the simulations

Component	Footprint (mm × mm)	Thickness/Height (mm)	Material	k (W m^{-1} K^{-1})	ρ (kg m^{-3}]	c_p (J kg^{-1} K^{-1})
Fin base	163 × 163	3 (H_b)	Aluminum	238	2700	900
Fins	—	10 (H_f)	Aluminum	238	2700	900
Heat source (die)	1 × 1	0.5	GaN	130	6150	490
Substrate	8 × 8	1.6	Copper	400	8960	385
TIM	8 × 8	0.02	—	3.5	—	—

channels that carry heat across the entire finned region before it is convected, maintaining that region at a high, nearly uniform temperature and minimizing the effective spreading resistance to the active surface. The _center baseline sinks retain ordinary, isotropic base conduction; therefore, although their fins occupy the same central footprint, they cannot reproduce this uniform delivery. Rather, their interior fins overheat, while the perforated periphery contributes little. Thus, the metastructure acts as a heat-spreading network tailored to the source distribution, which is consistent with the role of engineered high-conductivity routing in advanced heat-spreader designs.[38]

4.2. Surface-utilization efficiency

Figure 5 presents the efficiency η in **Equation 9** as a function of source power. As expected for a linear conduction–convection problem, η is nearly independent of the load for all the designs, but differs markedly between designs. The meta-fin attains η ≈ 0.38, exceeding those of the pin fin_all and plate fin_all baseline sinks (η ≈ 0.34) by more than 10%. Those of the two _center baseline sinks fall in between (η ≈ 0.36–0.37), which are higher than those of the _all sinks because their wasted peripheral surface has been removed, but they remain below that of the meta-fin. This ordering directly mirrors Figure 4: the η of the meta-fin is highest because only this sink heats its entire fin surface toward T_{max}. The theoretical upper limit is η = 1, corresponding to the ideal case in which the entire convecting surface reaches T_{max}. The lower value obtained here (η ≈ 0.38) reflects the spatial temperature gradients associated with the discrete heat sources and finite lateral heat spreading through the base.

4.3. Dissipated power

Figure 6 shows the convective heat rejected by each sink at a common transient instant as the source power increases from 5 to 25 W. The rejected heat rises monotonically with the source power for all the designs. Because the analysis is transient, the supplied energy is partitioned at each instant between what is convected to the air and what is stored as sensible heat in the sink itself. The rejected heat in Figure 6 is therefore an instantaneous transient quantity rather than the eventual steady-state balance, in which every design would ultimately reject its full input. Under the prescribed convective boundary condition, at the highest load, the meta-fin rejects ~15% more heat than pin fin_all and ~25% more heat than the other three sinks. Two mechanisms

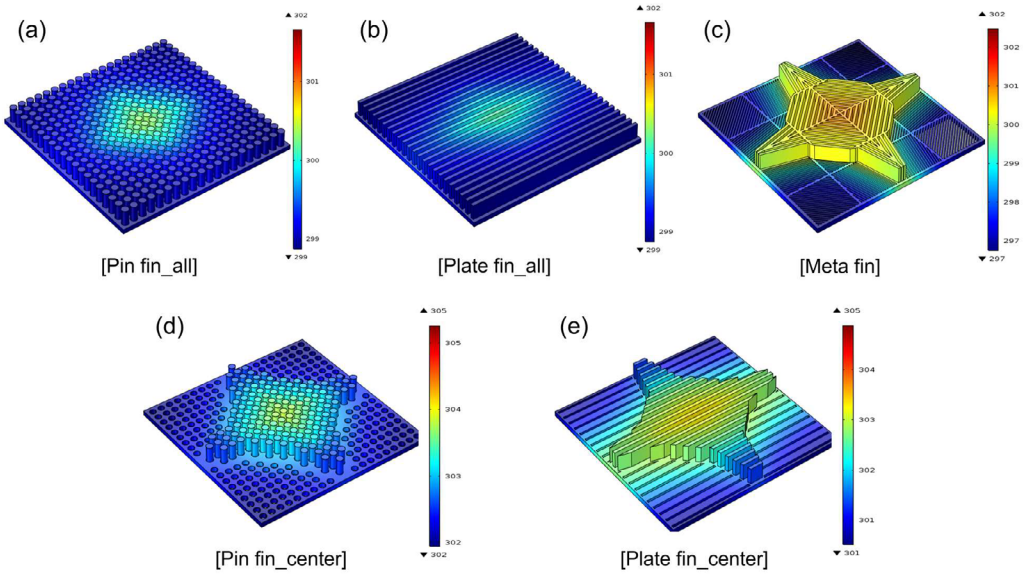

Figure 4. Simulated temperature fields of the five heat sinks at the common transient evaluation time: (a) pin fin_all, (b) plate fin_all, (c) meta-fin, (d) pin fin_center, and (e) plate fin_center. Only the meta-fin drives its entire fin region to a high, nearly uniform temperature, indicating full-surface convective utilization.

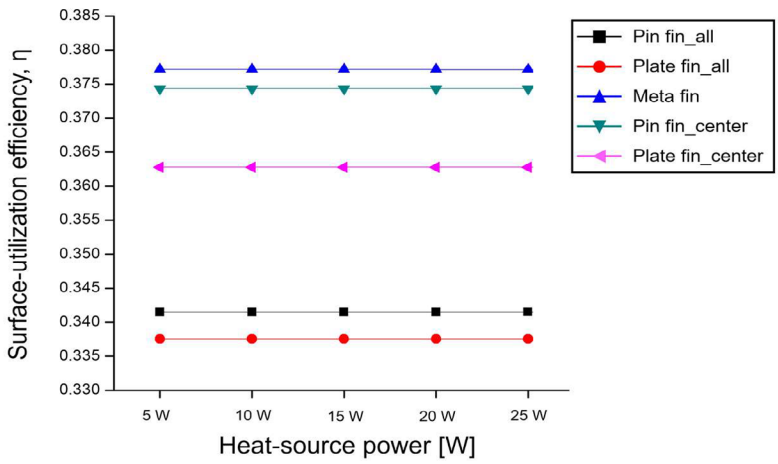

Figure 5. Surface-utilization efficiency η of each heat sink as a function of the heat-source power. η is essentially independent of the load; the meta-fin exceeds the conventional pin fin_all and plate fin_all baseline sinks by more than 10%.

produce these improvements together. First, relative to the heavier _all baseline sinks, the meta-fin diverts a larger share of the supplied energy into convection rather than warming its own larger thermal mass; therefore, at any given instant, it rejects more heat. Second, and more importantly, the meta-fin outperforms the mass-matched _center baseline sinks predominantly through heat routing. Specifically, by driving its entire fin surface toward a high, uniform temperature, it sustains a larger effective convective temperature difference, whereas the _center sinks leave the surface at intermediate temperatures. The fact that the meta-fin outperforms the volume- and weight-matched _center designs by ~25% indicates that the improvement is primarily an effect of routing the flux rather than an artifact of mass.

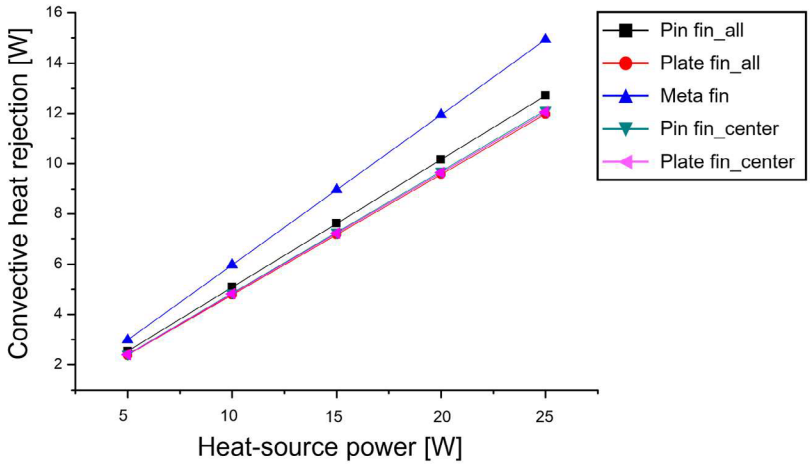

Figure 6. Convective heat rejected by each heat sink at the common transient instant as a function of the heat-source power under the prescribed convective boundary condition. The meta-fin rejects ~15% more than pin fin_all and ~25% more than the remaining designs at the highest load.

4.4. Volume and weight

Figure 7 and Tables 1 and 2 summarize the size and mass of each sink. Because the meta-fin carries fins only over the routed region, its volume (≈ 106 cm^3) and weight (≈ 0.30 kg) are approximately 46% and 45% smaller, respectively, than those of pin fin_all, and approximately 45% and 44% smaller than those of plate fin_all. The two _center baseline sinks were deliberately perforated to match the meta-fin, and their volumes and weights indeed differ by only ~1% (Table 2). Therefore, the performance advantage of the meta-fin over the mass-matched pin fin_center and plate fin_center baselines cannot be attributed to differences in material volume or mass.

It is useful to combine the dissipation and mass results into a single engineering figure of merit, namely, the heat rejected per unit mass (or volume), which is significant for portable and space-constrained systems. Under the prescribed convective boundary condition, relative to pin fin_all, the approximately 2.1-fold mass-normalized transient heat-rejection advantage can be decomposed into two contributions: the meta-fin exhibits ~15% higher absolute transient heat rejection (a factor of ~1.15), while its ~45% lower mass provides a mass-normalization factor of 1 / 0.55 ≈ 1.82. Their product gives 1.15 × 1.82 ≈ 2.1. Thus, the 2.1-fold value reflects the combined effects of enhanced transient heat rejection and reduced material mass rather than a 2.1-fold routing enhancement alone. In other words, the metastructured layout delivers a higher absolute performance from a sink that is nearly half the size and weight, benefitting only from redesigning the fin layout without changing the heat-sink material.

4.5. Deterministic heat-flux control and directional temperature contrast

Beyond raw dissipation, the routed layout provides explicit control over where heat is and is not allowed to flow, a valuable capability for creating spatially differentiated thermal zones and protecting temperature-sensitive neighboring regions. To quantify this property, we probed the surface temperature of each sink along three lines through the center—the x-axis, y-axis, and diagonal—at the probe locations shown in Figure 8a. Along the x- and y-axes (Figure 8b and 8c), the meta-fin behaves much like the other sinks because its fin field extends along both axes: the temperature is highest at the center and decreases outward, and the two _center baseline sinks run 3–4 K hotter at the center than the other three designs. However, the diagonal direction (Figure 8d) reveals the signature of the routed layout. The maximum-to-minimum temperature spread along the diagonal is only modest for the conventional sinks (2.00 K for pin fin_all, 1.57 K for plate fin_all, 2.15 K for pin fin_center, and 3.43 K for plate fin_center), whereas that of the meta-fin reaches 5.26 K—more than 2.5× those of the two full-footprint baseline sinks and ~1.5× that of the next-highest design (plate fin_center).

This large diagonal gradient is the direct fingerprint of heat-flux routing: the shield channels heat into the finned region and starves the diagonal insulating gaps, producing sharply defined hot and cold zones. In an electronic assembly, this means that heat can be preferentially directed away from regions containing temperature-sensitive components, providing a degree of spatial thermal control that is difficult to achieve with a conventional isotropically spreading sink.

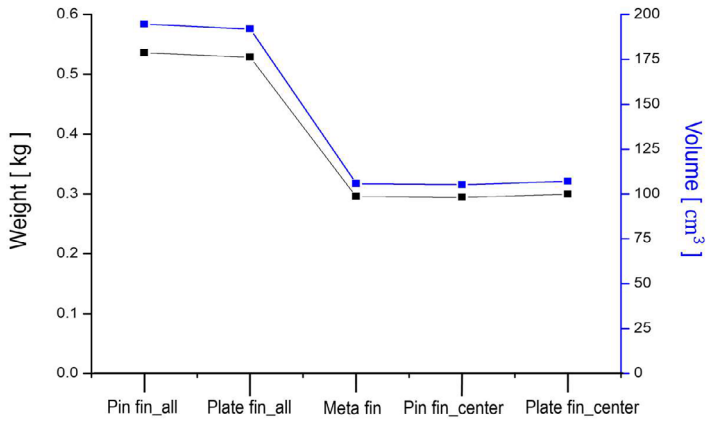

Figure 7. Weight and volume of the five heat sinks. The meta-fin is ~45% lighter and smaller than the full-footprint baseline sinks, while the _center baseline sinks are matched to the meta-fin in volume and weight.

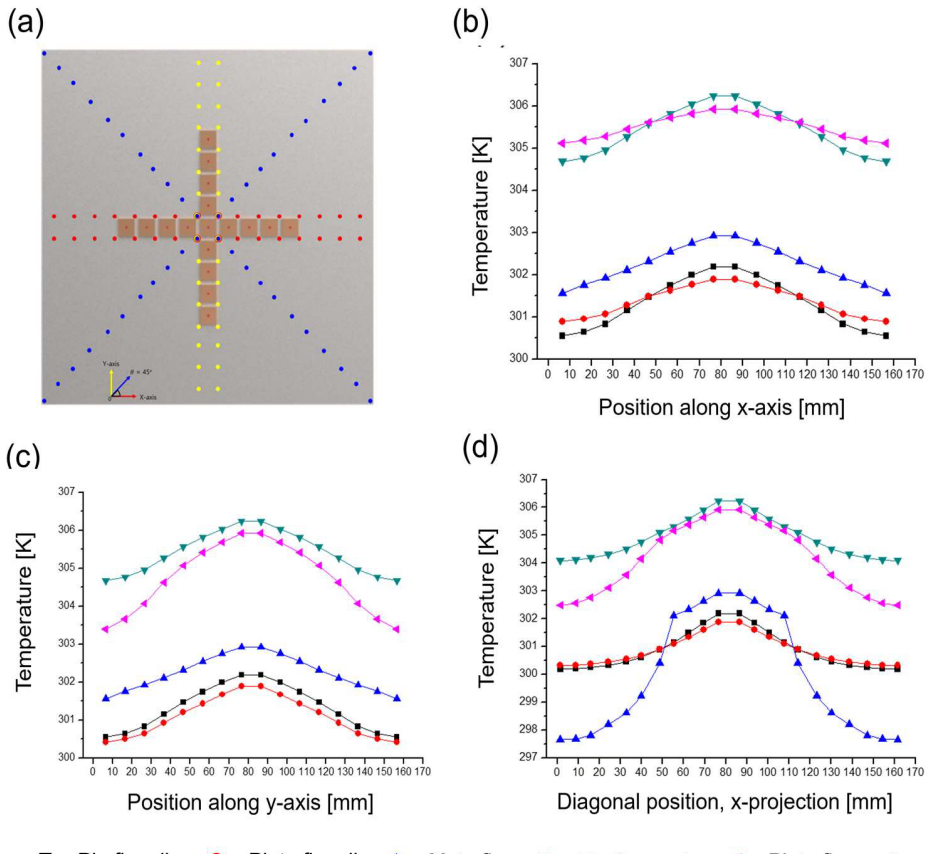

Figure 8. Directional surface-temperature analysis. (a) Probe locations over the 17-source array (x-axis, red; y-axis, yellow; diagonal, blue). Temperature profiles measured along the (b) x-axis, (c) y-axis, and (d) diagonal (θ = 45°) of each heat sink, where the diagonal profile is plotted against the probe position projected onto the x-axis. Along the diagonal, the meta-fin shows a maximum-to-minimum difference (5.26 K) substantially larger than those of all conventional designs (1.57–3.43 K), which is the signature of deterministic heat-flux routing.

Taken together, these results show that matching the fin layout to a thermal-shield heat-flux pattern transforms a heat sink from a passive isotropic spreader into an effective heat-flux-routing device, improving both the surface-utilization efficiency and the transient heat rejection, while nearly halving the size and weight.

The present strategy is complementary to heat-path optimization, topology optimization, and high-conductivity heat-spreading approaches.[7,8] Unlike methods that primarily optimize thermal resistance or promote broad heat spreading, the thermal-shield concept provides deterministic control over both preferential heat-flow paths and thermally suppressed regions. This capability is particularly useful for multi-hotspot systems where heat dissipation, thermal crosstalk, and localized temperature constraints must be managed simultaneously. Moreover, the metastructure-defined routing domain could be combined with topology optimization in future designs to further optimize the fin geometry and three-dimensional heat-transfer pathways. Looking ahead, the non-standard fin and void arrangement considered here can be realized using metal additive manufacturing or precision CNC machining, with additive manufacturing offering particular flexibility for integrating the routed fin field and, ultimately, the layered unit-cell shifters into a single component. For additive-manufacturing implementation, build orientation should be selected to minimize unsupported features and dimensional distortion, while as-built surface roughness and geometric deviations may alter the effective surface area and local convective behavior relative to the idealized geometry considered here. The use of a single metal with engineered air gaps may nevertheless simplify material selection and fabrication relative to multi-material metastructures.[4,9,40,43]

4.6. Modeling scope and outlook

Several modeling choices define the scope within which the present conclusions hold, and they are summarized here to clarify how the findings generalize. First, every exposed surface is assigned the same constant, surface-averaged heat-transfer coefficient h. In an actual heat sink, the local coefficient varies with surface orientation, boundary-layer development, fin spacing, and channel confinement; therefore, the denser meta-fin geometry may experience a greater local convective penalty than the more widely spaced baseline designs. The present prescribed-h model does not resolve these geometry-dependent airflow effects. Instead, consistent with the primary objective of this study, it provides a common external boundary condition for isolating how the different heat-routing and fin-layout strategies affect the solid-side thermal response and utilization of the available convecting surface. The adopted h = 10 W m^{-2} K^{-1} represents a prescribed moderate convection condition rather than a flow-resolved prediction of local natural convection. Accordingly, the quantitative performance differences reported here apply to this prescribed-convection framework and should not be interpreted as universal natural-convection performance gains. Determining the influence of geometry-dependent local convection requires a buoyancy-coupled conjugate heat-transfer model or corresponding experimental measurements.

Second, the heat-rejection magnitudes are transient-instant quantities and should be read comparatively rather than as steady-state ratings. Third, a single multi-hotspot layout, material combination, fin-geometry range, and thermal-shield unit-cell configuration were considered; therefore, the quantitative gains may vary with parameters such as the constituent conductivity ratio, fin dimensions, and unit-cell geometry. Nevertheless, the small Biot number and fin parameter under the present conditions indicate only minor internal temperature gradients within the aluminum fins, while the large unit-cell anisotropy ratio places the thermal shield in a strong-routing regime. The present comparison therefore primarily isolates the layout-level effect of routing heat into a compact, highly utilized fin field. Finally, the present heat-sink performance comparison is numerical. The fabricated structure shown in Figure 1a is a fin-free thermal-shield prototype demonstrating the physical realization of the underlying heat-routing concept, whereas the five finned heat-sink configurations in Figure 2 are numerical designs. Accordingly, the quantitative performance differences reported here should be interpreted within the computational framework described above. Taken together, these considerations delimit the quantitative scope of the results without affecting the central, layout-level finding that routing heat into a compact finned region improves dissipation per unit mass and volume.

5. Conclusions

Transient 3D heat-transfer simulations showed that matching the fin layout of a heat sink to a thermal-shield heat-flux pattern can convert it from a passive isotropic spreader into an effective heat-flux-routing device. The key findings are as follows: (i) The thermal-shield concept, derived from manufacturable unit-cell shifters comprising a metal and simple air gaps, determines where the heat of a multi-hotspot source array is routed, allowing fins to be installed only where they are thermally productive. (ii) The resulting meta-fin sink essentially heats its entire fin surface, raising the surface-utilization efficiency by more

than 10% over that of conventional pin- and plate-fin sinks. (iii) It rejects 15%–25% more heat than the baseline sinks—including baseline sinks matched in volume and weight—indicating that the gain is primarily an effect of this routing rather than an artifact of size or mass. (iv) Finally, it does so while being ~45% smaller and lighter, approximately doubling its heat rejection per unit mass and volume. The routed layout also provides deterministic control of the on-chip temperature landscape, producing a diagonal temperature contrast more than 2.5× that of the conventional full-footprint sinks. This feature provides a means to create spatially differentiated thermal zones within a multi-hotspot heat sink.

Because these benefits were attained by redesigning the fin layout rather than introducing new materials or processes, the meta-fin is directly compatible with existing heat-sink manufacturing and offers a practical path toward lightweight, crosstalk-aware thermal management of multi-hotspot electronics. However, the present results were obtained under a prescribed constant-h convective boundary condition and at a transient operating point; therefore, the quantitative gains should be understood comparatively. Confirming these findings under realistic conditions is the central task ahead. Future work will accordingly extend the concept to buoyancy-coupled and forced- and mixed-convection regimes and integrate it with topology optimization and additive manufacturing for fully 3D heat routing. In particular, the rapid progress of metal and multi-material 3D printing[7,40,41] makes the direct fabrication of such metastructured heat sinks—including their layered metal–air unit cells—increasingly feasible; we therefore anticipate that additive manufacturing will be a key enabler for the demonstration and eventual deployment of this new class of heat-sink form factors.

Acknowledgments

None.

Funding

This work was supported by an Agency for Defense Development of Korea (ADD) grant (915050201), National Research Foundation of Korea (NRF) funded by the Korean government (Ministry of Science and ICT) (2023R1A2C2006407, 2020R1A5A1018153), and Korea Evaluation Institute of Industrial Technology (KEIT) grant funded by the Korea government (MOTIE) (No. RS-2024-00433288).

Conflict of interest

Wonjoon Choi is an Editorial Board Member of this journal but was not in any way involved in the editorial and peer-review process conducted for this paper, directly or indirectly. Separately, other authors declared that they have no known competing financial interests or personal relationships that could have influenced the work reported in this paper.

Author contributions

Conceptualization: Kyungbeom Seo, Wonjoon Choi
Formal analysis: Kyungbeom Seo, Sooyeon Ji, Myounggi Hong, Yeonbin Seong, Yong Choi
Investigation: Kyungbeom Seo, Sooyeon Ji, Myounggi Hong
Methodology: Kyungbeom Seo, Yeonbin Seong, Yong Choi, Hwanju Lim
Project administration: Wonjoon Choi
Supervision: Wonjoon Choi
Writing–original draft: Kyungbeom Seo, Sooyeon Ji, Myounggi Hong, Yeonbin Seong Wonjoon Choi
Writing–review & editing: All authors

Ethics approval and consent to participate

Not applicable.

Consent for publication

Not applicable.

Availability of data

The authors confirm that the data supporting the findings of this study are available within the article.

References

1. Li Y, Roux S, Castelain C, Fan Y, Luo L. Design and optimization of heat sinks for the liquid cooling of electronics with multiple heat sources: A literature review. *Energies*. 2023;16(22):7468.

   doi: 10.3390/en16227468

2. Li Z, Luo H, Jiang Y, *et al.* Comprehensive review and future prospects on chip-scale thermal management: Core of data center's thermal management. *Appl Therm Eng*. 2024;251:123612.

   doi: 10.1016/j.applthermaleng.2024.123612

3. Rahman MA, Hasnain SMM, Paramasivam P, Ayanie AG. Advancing thermal management in electronics: A review of innovative heat sink designs and optimization techniques. *RSC Adv*. 2024;14(43):31291-31319.

   doi: 10.1039/D4RA05845C

4. Kim JC, Ren Z, Yuksel A, *et al.* Recent advances in thermal metamaterials and their future applications for electronics packaging. *J Electron Packag*. 2021;143(1):010801.

   doi: 10.1115/1.4047414

5. Nair V, Baby A, Anoop MB, Indrajith S, Murali M, Nair MB. A comprehensive review of air-cooled heat sinks for thermal

management of electronic devices. *Int Commun Heat Mass Transf*. 2024;159:108055.

doi: 10.1016/j.icheatmasstransfer.2024.108055

6. Hu X, Gong X, Zhu F, Xing X, Li Z, Zhang X. Thermal analysis and optimization of metal foam PCM-based heat sink for thermal management of electronic devices. *Renew Energy*. 2023;212:227-237.

doi: 10.1016/j.renene.2023.05.021

7. Sun S, Rankouhi B, Thoma DJ, *et al.* Topology optimization, additive manufacturing and thermohydraulic testing of heat sinks. *Int J Heat Mass Transf*. 2024;224:125281.

doi: 10.1016/j.ijheatmasstransfer.2024.125281

8. Luo JW, Chen L, Xia Y, Zheng X, Tao WQ. Three-dimensional multi-scale topology optimization of porous heat sink with predetermined unit cells for natural convection heat transfer. *Int J Heat Mass Transf*. 2024;225:125398.

doi: 10.1016/j.ijheatmasstransfer.2024.125398

9. Ji S, Choi J, Hong M, *et al.* Recent advances in thermal management via additive manufacturing. *Eng Sci Addit Manuf*. 2025;1(3):025260016.

doi: 10.36922/ESAM025260016

10. Careri F, Khan RHU, Todd C, Attallah MM. Additive manufacturing of heat exchangers in aerospace applications: A review. *Appl Therm Eng*. 2023;235:121387.

doi: 10.1016/j.applthermaleng.2023.121387

11. Liu C, Zhang M, Bi G, *et al.* Research on comprehensive heat dissipation characteristics of AlSi7Mg TPMS heat sinks manufactured by laser powder bed fusion. *Appl Therm Eng*. 2025;261:124941.

doi: 10.1016/j.applthermaleng.2024.124941

12. Ozguc S, Teague TFG, Pan L, Weibel JA. Experimental study of topology optimized, additively manufactured microchannel heat sinks designed using a homogenization approach. *Int J Heat Mass Transf*. 2023;209:124108.

doi: 10.1016/j.ijheatmasstransfer.2023.124108

13. Gallorini E, Hélie J, Piscaglia F. A multi-region adjoint-based solver for topology optimization in conjugate heat transfer problems. *Comput Fluids*. 2023;266:106042.

doi: 10.1016/j.compfluid.2023.106042

14. Sahin I, Moya C, Mollaali A, Lin G, Paniagua G. Deep operator learning-based surrogate models with uncertainty quantification for optimizing internal cooling channel rib profiles. *Int J Heat Mass Transf*. 2024;219:124813.

doi: 10.1016/j.ijheatmasstransfer.2023.124813

15. Song C, Liang X. Design optimization of 2D cross-flow heat exchanger using shape coupling neural network. *Int J Heat Mass Transf*. 2025;253:127616.

doi: 10.1016/j.ijheatmasstransfer.2025.127616

16. Lamotte-Dawaghreh J, Herring J, Pundla SA, *et al.* Electrochemical additive manufacturing-based design of a heat sink for single-phase natural convection immersion cooling application. *J Electron Packag*. 2024;146(4):041113.

doi: 10.1115/1.4065987

17. Zhou W, Dong K, Sun Q, *et al.* Research progress of the liquid cold plate cooling technology for server electronic chips: A review. *Int J Energy Res*. 2022;46(9):11574-11595.

doi: 10.1002/er.7979

18. Dixit A, Maithani R, Sharma S. Enhancing electronic system cooling: Exploring minichannel heat sink solutions. *J Therm Anal Calorim*. 2025;150:5357-5407.

doi: 10.1007/s10973-025-14118-7

19. Fan CZ, Gao Y, Huang JP. Shaped graded materials with an apparent negative thermal conductivity. *Appl Phys Lett*. 2008;92(25):251907.

doi: 10.1063/1.2951600

20. Pendry JB, Schurig D, Smith DR. Controlling electromagnetic fields. *Science*. 2006;312(5781):1780-1782.

doi: 10.1126/science.1125907

21. Cummer SA, Christensen J, Alù A. Controlling sound with acoustic metamaterials. *Nat Rev Mater*. 2016;1:16001.

doi: 10.1038/natrevmats.2016.1

22. Schurig D, Mock JJ, Justice BJ, *et al.* Metamaterial electromagnetic cloak at microwave frequencies. *Science*. 2006;314(5801):977-980.

doi: 10.1126/science.1133628

23. Zhang Z, Xu L, Qu T, *et al.* Diffusion metamaterials. *Nat Rev Phys*. 2023;5(4):218-235.

doi: 10.1038/s42254-023-00565-4

24. Li Y, Li W, Han T, *et al.* Transforming heat transfer with thermal metamaterials and devices. *Nat Rev Mater*. 2021;6:488-507.

doi: 10.1038/s41578-021-00283-2

25. Narayana S, Sato Y. Heat flux manipulation with engineered thermal materials. *Phys Rev Lett*. 2012;108(21):214303.

doi: 10.1103/PhysRevLett.108.214303

26. Han T, Bai X, Gao D, Thong JTL, Li B, Qiu CW. Experimental demonstration of a bilayer thermal cloak. *Phys Rev Lett*. 2014;112(5):054302.

doi: 10.1103/PhysRevLett.112.054302

27. Yang F, Tian B, Xu L, Huang J. Experimental demonstration of thermal chameleon-like rotators with transformation-invariant metamaterials. *Phys Rev Appl*. 2020;14(5):054024.

doi: 10.1103/PhysRevApplied.14.054024

28. Xu LJ, Huang JP. *Transformation Thermotics and Extended*

Theories: Inside and Outside Metamaterials. Singapore: Springer; 2023.

doi: 10.1007/978-981-19-5908-0

29. Fan C, Wu CL, Wang Y, Wang B, Wang J. Thermal metamaterials: From static to dynamic heat manipulation. *Phys Rep*. 2024;1077:1-111.

doi: 10.1016/j.physrep.2024.05.004

30. Qiu Y, Nomura M, Zhang Z, *et al.* Roadmap on thermodynamics and thermal metamaterials. *Front Phys*. 2025;20(6):65500.

doi: 10.15302/frontphys.2025.065500

31. Li W, Sigmund O, Zhang XS. Analytical realization of complex thermal meta-devices. *Nat Commun*. 2024;15:5527.

doi: 10.1038/s41467-024-49630-1

32. Yang F, Zhang Z, Xu L, *et al.* Controlling mass and energy diffusion with metamaterials. *Rev Mod Phys*. 2024;96:015002.

doi: 10.1103/RevModPhys.96.015002

33. Li ZY, Ma TX, Yan D, *et al.* Non-Fourier thermal focusing by gradient thermal metamaterials based on the Cattaneo-Vernotte model. *J Appl Phys*. 2024;136(19):193106.

doi: 10.1063/5.0228819

34. Mclean H, Davies FH, Taylor NT, Hepplestone SP. Thermal metamaterials for enhanced non-Fourier heat transport. *npj Metamaterials*. 2025;1:7.

doi: 10.1038/s44455-025-00008-3

35. Yao NZ, Wang H, Wang B, Wang X, Huang JP. Convective thermal cloaks with homogeneous and isotropic parameters and drag-free characteristics for viscous potential flows. *iScience*. 2022;25(11):105461.

doi: 10.1016/j.isci.2022.105461

36. Dai GL, Zhou Y, Wang J, Yang F, Qu T, Huang JP. Convective cloak in Hele-Shaw cells with bilayer structures: Hiding objects from heat and fluid motion simultaneously. *Phys Rev Appl*. 2022;17(4):044006.

doi: 10.1103/PhysRevApplied.17.044006

37. Ju R, Xu G, Xu L, *et al.* Convective thermal metamaterials: Exploring high-efficiency, directional, and wave-like heat transfer. *Adv Mater*. 2023;35(23):e2209123.

doi: 10.1002/adma.202209123

38. Xu B, Liao Y, Fang Z, *et al.* Ultra-high-performance heat spreader based on a graphite architecture with three-dimensional thermal routing. *Cell Rep Phys Sci*. 2021;2(11):100621.

doi: 10.1016/j.xcrp.2021.100621

39. Zhu C, Bamidele EA, Shen X, Zhu G, Li B. Machine learning aided design and optimization of thermal metamaterials. *Chem Rev*. 2024;124(7):4258-4331.

doi: 10.1021/acs.chemrev.3c00708

40. Samad SN, Griffis J, Manogharan G, Kouraytem N. Multi-material additive manufacturing of metals: A review of structures and mechanical characteristics. *Eng Sci Addit Manuf*. 2025;1(2):025180010.

doi: 10.36922/ESAM025180010

41. Nipu SMA, Tang T, Joralmon D, *et al.* Advances and perspectives in multi-material additive manufacturing of heterogenous metal-polymer components. *npj Adv Manuf*. 2025;2:31.

doi: 10.1038/s44334-025-00045-w

42. Subeshan B, Hamzat AK, Asmatulu E. Fabricating three-dimensional metamaterials using additive manufacturing: An overview. *J Manuf Mater Process*. 2025;9(10):343.

doi: 10.3390/jmmp9100343

43. Park G, Kang S, Lee H, Choi W. Tunable multifunctional thermal metamaterials: Manipulation of local heat flux via assembly of unit-cell thermal shifters. *Sci Rep*. 2017;7:41000.

doi: 10.1038/srep41000

44. Jang D, Yu SH, Lee KS. Multidisciplinary optimization of a pin-fin radial heat sink for LED lighting applications. *Int J Heat Mass Transf*. 2012;55(4):515-521.

doi: 10.1016/j.ijheatmasstransfer.2011.11.016